Bare-Eye View at the Nanoscale: New Visual Interferometric Multi-Indicator (VIMI)

Nikolaos T. Panagiotopoulos,[†] Panos Patsalas,*[,‡] Constantinos Prouskas,[‡] Georgios P. Dimitrakopulos,[§] Philomela Komninou,[§] Theodoros Karakostas,[§] Adrian P. Tighe,[||] and Elefterios Lidorikis*[,‡]

Department of Physics and Department of Materials Science and Engineering, University of Ioannina, GR-45110 Ioannina, Greece, Department of Physics, Aristotle University of Thessaloniki, GR-54124 Thessaloniki, Greece, and ESTEC Materials, Physics and Chemistry Section, European Space Agency, Keplerlaan 1, 2200AG Noordwijk, The Netherlands

ABSTRACT By exploiting the interferometric antireflection action of a probe sample, consisting of a diamond-like carbon (DLC) film grown on Si, combined with a specific illumination spectrum, we designed and constructed an optical device for the visual remote sensing of radiation (either plasma or atomic oxygen) and for the visual inspection of adsorbed organic contamination as thin as a few molecular layers. The capabilities of this new visual interferometric multi-indicator (VIMI) enable the bare-eye color detection of thickness changes on the order of a few nanometers without the intervention of any instrumental or computer interface.

KEYWORDS: interferometry • visual inspection • contamination sensors • radiation sensors • diamond-like carbon

1. INTRODUCTION

Interferometric methods have emerged as powerful tools in optical sensing and imaging (1−13), achieving high spatial and optical-density resolution. Optical interferometry is based on phase changes of light, thus being able to probe subwavelength features on the sample's surface stretching the limits of applications well below the 0.5 μm diffraction limit of visible light. Ultimate paradigms of interferometric imaging include the visualization of single graphene layers (5), virus detection (8), strain measurements in Si electronic devices (9), and the measurement of nanoscale gaps (13). To enhance the interference phenomena, researchers typically use a laser source that provides coherent radiation in high-resolution interferometric devices. Highly sophisticated optical set up and data acquisition electronics as well as software-controlled imaging are implemented in both white-light and laser interferometry. Therefore, the direct imaging of nanoscale objects is not possible without the use of appropriate instrumentation and user-computer interface. There are cases, however, where a sophisticated setup is not possible, as for example when monitoring surface changes of large devices and structures (e.g., airplanes or cars), or when the monitoring needs to be done in harsh environments (e.g., inside a growth chamber). In addition, by its own merit a quick semiquantitative inspection may suffice and be more practical, for example, for verification of nanoscale thickness changes during growth and/or surface functionalization, or for warning against environmental contamination. It is thus highly beneficial to develop a fully remote and passive semiquantitative inspection method.

In this work, we present the design, construction, and operation of a new visual interferometric indicator of multiple functions that provides direct bare-eye information, i.e., visible color change, when nanoscale changes take place, such as for example the adsorption of a few organic contaminant monolayers on the surface. In addition, when coupled with a spectrometer, it provides quantitative measurements with subnanometer accuracy. This Visual Interferometric Multi Indicator (VIMI) is tested for various space-relevant functions and applications (14−18), such as: (1) thickness monitor for film growth; (2) detection of radiation, such as plasma or atomic oxygen (ATOX) (14−16), through the detection of erosion of a radiation-sensitive surface; (3) sensing the adsorption of an environmental organic contaminant on a surface (17).

For the implementation and construction of VIMI, a diamond-like carbon (DLC) antireflection coating-layer on Si is used, combined with a standard, commercial red-green-blue (RGB) light-emitting diode (LED) assembly. DLC is a well-known engineering material (19) that exhibits a vast range of optical properties depending on the sp^3/sp^2 bond ratio and hydrogen content (20−30), thus being appropriate for various optical applications. In addition, DLC has been also considered for various space-related applications (31−36).

2. DESIGN OF VIMI

In this section, we demonstrate the basic operation principles of the proposed coating-indicator. As with any

* Corresponding author. Tel: +30-26510-08592 (P.P.); +30-26510-07146 (E.L.). Fax: +30-26510-07034 (P.P.); +30-26510-07034 (E.L.). E-mail: ppats@cc.uoi.gr and ppats@physics.auth.gr (P.P.); elidorik@cc.uoi.gr. (E.L.).
Received for review June 19, 2010 and accepted October 11, 2010
† Department of Physics, University of Ioannina.
‡ Department of Materials Science and Engineering, University of Ioannina.
§ Aristotle University of Thessaloniki.
|| European Space Agency.
DOI: 10.1021/am100532b
2010 American Chemical Society

Published on Web 11/04/2010

indicator/sensor, and in order to maximize sensitivity, the sensing element (e.g., a thin film on top of Si) has to be tuned so that the measurement (reflectance) approaches zero at the sensor healthy state, so that any small change in thickness or composition will cause a significant measurable contrast. Different film materials have a different response to various effects, and thus different sensing capabilities (e.g., DLC is particularly sensitive to ATOX while AlN is not). For simplicity we adopt the DLC/Si film—substrate system. The gauge quantity is reflectance, which for a general film/substrate system at normal incidence is given by

$$R = \left| \frac{n_{film}(n_{sub} - 1)\cos kt - i(n_{film}^2 - n_{sub})\sin kt}{n_{film}(n_{sub} + 1)\cos kt - i(n_{film}^2 + n_{sub})\sin kt} \right|^2 \quad (1)$$

where n_{film} and n_{sub} are the (generally complex) refractive indices of an antireflection coating and of the substrate respectively, t is the film thickness, $k = 2\pi n_{film}/\lambda$, and λ the wavelength in vacuum. The reflectance is tuned to be exponentially small at 635 nm. For transparent film and substrate this is achieved when the conditions

$$n_{film} = \sqrt{n_{sub}}$$

$$t_{film} = \lambda/4n_{film} \quad (2)$$

are fulfilled. Here, however, we use an n-doped Si substrate which at 635 nm has $\tilde{n}_{Si} = n_{Si} + i\kappa_{Si} = 3.92 + i0.07$ (37). For a transparent film the above conditions are modified to $n_{film} = [n_{Si} + \kappa_{Si}^2/(n_{Si} - 1)]^{1/2}$, $t_{film} = \lambda/(2\pi n_{film})\arctan [n_{film}(n_{Si} - 1)/\kappa_{Si}]$. Also, the DLC films are absorbing and so the antireflection conditions are further modified, albeit toward the opposite direction. A closed form expression is not available and so optimization must be done numerically, however, eq 2 remains a fair guide, i.e., $n_{DLC} \approx 1.98$ and $t \approx 80.2$ nm.

The DLC refractive indices span the range between 1.6 and 2.6 (20); therefore, the intermediate value $n_{DLC} \approx 1.98$ is easily achieved for DLC films grown by plasma-enhanced Chemical Vapor Deposition (PECVD) as shown in Figure 1. In this figure, the spectral variation of the refractive index of several DLC films grown by PECVD are compared to the square root of the refractive index of the standard Si substrate (both measured using optical reflectance spectroscopy, ORS). Note that the approximate antireflection condition of eq 2 is fulfilled at $\lambda = 635$ nm. The bottom inset shows the corresponding extinction coefficient for the films. Overall, excellent reproducibility is obtained. The top inset shows a cross-section transmission electron microscopy (TEM) image demonstrating the morphology of such a DLC/Si system.

On such a film, normally incident light of $\lambda = 635$ nm will have infinitesimal reflectance. In order to visually inspect small thickness changes due to either contaminant adsorption or DLC erosion (e.g., from exposure to plasma/radiation), we need to illuminate with a spectral shape that takes advantage of the specific reflectance response. We choose the spectral shape of Figure 2, i.e. a strong line at 635 nm (red) and a weak line at 535 nm (green), utilizing the ProLight PL6N-3LFX 3W Star RGB Power LED (38). Upon reflectance, at the healthy state the apparent color will be green (zero red reflection), Figure 3a, and as the film thickness changes shifting away from the antireflection condition, more red will be reflected, as shown in Figure 3b, changing the reflected composite color from green to yellow, orange, and red. The reflected color is easily visible by bare eyes; however, it can be also quantified by using Adobe RGB (1998) color image encoding (39). The sensitivity of the indicator is determined by the interferometric antireflective action of the DLC/Si; the less reflectance at 635 nm (ideally <1 × 10^{-4}), the more sensitive the indicator will be. This requirement sets the fabrication standards.

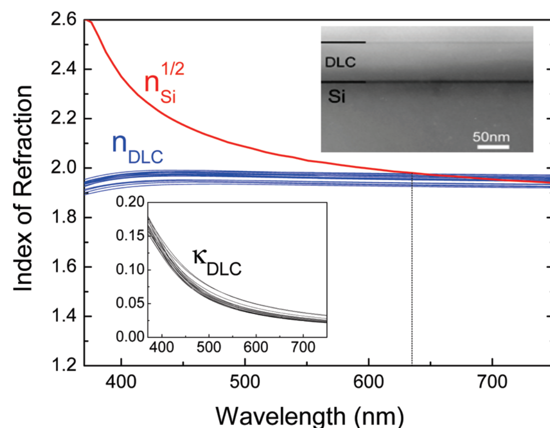

FIGURE 1. Experimental refractive indices of Si and several DLC samples determined by ORS. Note that the approximate $n_{DLC} = n_{Si}^{1/2}$ condition is satisfied at around 635 nm. The bottom inset shows the corresponding extinction coefficients, while the top inset shows a cross-section TEM image of a representative DLC/Si system, which is used in the VIMI.

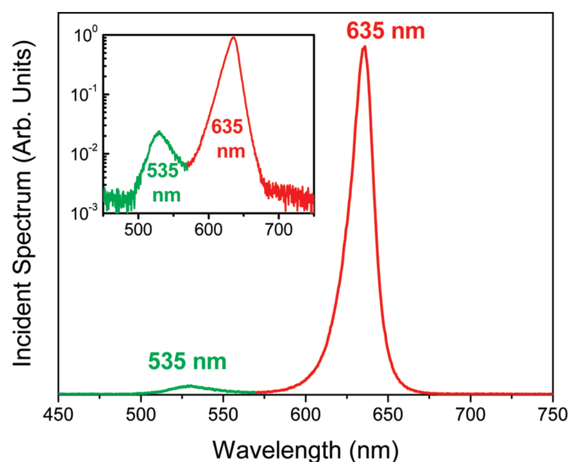

FIGURE 2. Incident spectrum consists of a strong red line at 635 nm and a weak green line at 535 nm emitted from a commercial LED. The integral peak intensity ratio between the two is 40:1. The more the integral intensity contrast, the more sensitive VIMI is.

3. FABRICATION AND TESTING DETAILS

The DLC films were deposited on commercial, Czochralski-grown, n-type Si (001) wafers by PECVD in a RF parallel

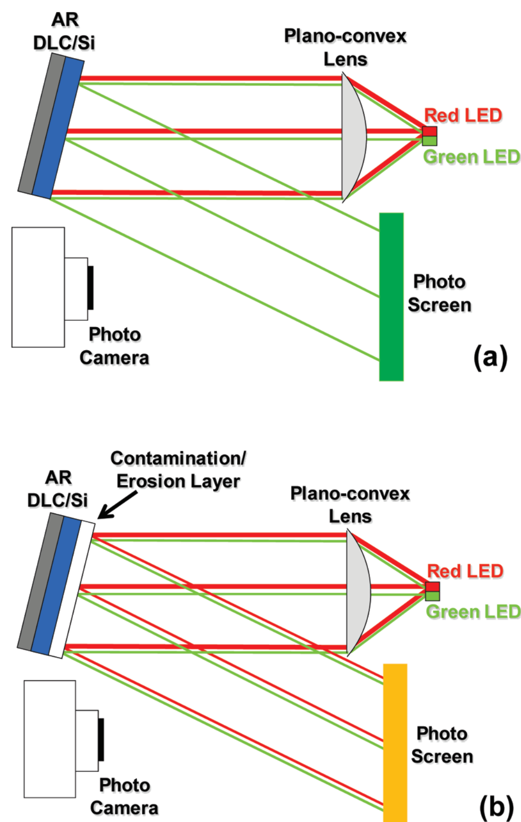

FIGURE 3. Simple optical set up used for the VIMI. (a) Healthy condition: strong green apparent reflection due to the antireflective action of the DLC/Si system. (b) Contamination sensing: upon adsorption of an ultrathin contamination layer the antireflection condition at 635 nm changes resulting to a change of the apparent composite color reflection, with specific RGB coordinates, which can be viewed by bare eyes.

plate high-vacuum ($P_b < 2 \times 10^{-6}$ mbar) reactor at room temperature. The substrates were cleaned by standard ultrasonic baths of tetrachloroethylene, acetone, and methanol, rinsed by deionized water, and dried by pure (electronic grade) N_2 gas shower prior to introduction to the reactor, in order to remove the organic contaminants on the surface. In the reactor the wafers were plasma-etched with Ar^+ (rf Power 60 W, Ar flow 50 sccm, working pressure 0.16 mbar) for 15 min.

The DLC growth was performed using gas precursor mixtures of Ar/C_2H_2 (99.999%/99.6% purity respectively) at flow 5/5 sccm respectively, keeping the operating pressure at $(4.5 \pm 0.5) \times 10^{-2}$ mbar. The RF (13.56 MHz) power is connected to the reactor electrode through an autotuned matching network. The RF power used for the particular DLC presented in Figure 1 was 60 W.

The optical properties of the DLC films were tested using optical reflectance spectroscopy (ORS) in the 370 to 780 nm (1.59–3.35 eV) spectral range. The density of the films has been determined by reflection electron energy loss spectroscopy (40) using an electron gun and a concentric cylindrical mirror analyzer. The specific DLC/Si films used for the VIMI have $n_{DLC} = 1.94-1.98$ and density $\rho = 1.6$ g/cm^3, values that are consistent with previous works (20).

Specimens for cross-section transmission electron microscopy (TEM) observations were prepared using mechanical polishing followed by Ar-ion milling up to electron transparency. TEM observations, both in conventional and high-resolution mode, were performed in a JEOL 2011 TEM operated at 200 kV.

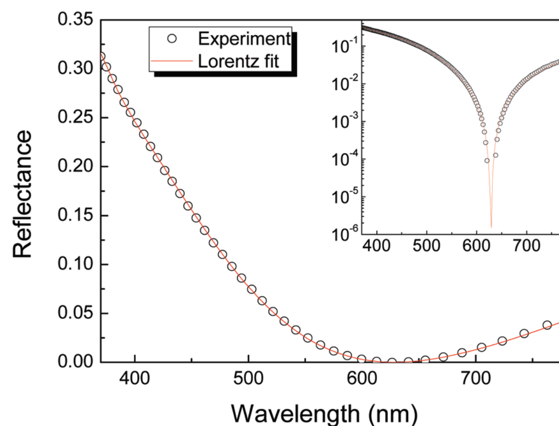

FIGURE 4. Experimental points of optical reflectance (points) and the Lorentz fit (line). The inset shows the optical reflectance in log-scale around the antireflection point of $\lambda = 635$ nm.

4. RESULTS AND DISCUSSION

The first step of our study is the accurate determination of the optical response of the DLC/Si system, which is being used as an integral part of VIMI. The optical properties were tested using spectral reflectance measurements, which has been modeled based on the corresponding calculated dielectric function of DLC. The dielectric function of DLC was analyzed using the Lorentz model to describe the $\pi-\pi^*$ interband transition (20, 41)

$$\tilde{\varepsilon}(\omega) = \varepsilon_\infty + \frac{f\omega_0^2}{\omega_0^2 - \omega^2 - i\gamma\omega} \qquad (3)$$

where ε_∞ is a background constant, larger than unity predominantly due to the $\sigma-\sigma^*$ interband transition (beyond the experimental spectral range) (20). The Lorentz oscillator is located at an energy position $E_0 = \hbar\omega_0$, with strength f and damping (broadening) factor γ. The ORS spectra were fitted combining eq 3 with the reflectance of a thin-film/substrate system of eq 1, where $\tilde{\varepsilon}^{1/2} = \tilde{n}_{DLC} = n_{DLC} + i\kappa_{DLC}$. The fit is performed using all the reflectance data, with unknowns the ε_∞, f, ω_o, γ, and DLC thickness t. The use of spectral reflectance measurements (i.e., a set of experimental points at 176 different wavelengths) enables the statistically reliable determination of the five (5) fit parameters (ε_∞, f, ω_o, γ, and DLC thickness t). Figure 4 shows a typical ORS spectrum of a DLC/Si sample. The points are the reflectance experimental data in the range between 370 and 780 nm, whereas the solid line stands for the best fit with eq 3. At $\lambda = 635$ nm, the reflectance is infinitesimally small, as shown in the inset of Figure 4, demonstrating reflectance values well smaller than 1×10^{-4} (the experimental points cannot be less than 1×10^{-5} due to the limitation of the electronic noise of the used spectrometer); an extrapolation of the experimental points at $\lambda = 635$ nm yields reflectance values

Table 1. Measured Reflectance Dip and the Fitted Film Thickness (t), Lorentz Oscillator Parameters and Complex Refractive Index at 635 nm for the Samples S1−S9

sample	experiment dip (nm)	Lorentz fit results						
		t (nm)	ε_∞	γ	ω_0 (eV)	f	n	κ
S1	629	81.6	3.38	1.80	3.71	0.31	1.94	0.035
S2	643	83.9	3.35	1.79	3.61	0.32	1.94	0.039
S3	664	86.4	3.40	1.64	3.63	0.28	1.94	0.031
S4	673	87.1	3.44	1.56	3.57	0.27	1.95	0.030
S5	681	87.5	3.41	1.70	3.87	0.37	1.97	0.035
S6	725	93.7	3.46	1.53	3.64	0.30	1.96	0.031
S7	731	94.9	3.42	1.55	3.67	0.32	1.96	0.032
S8	575	73.8	3.42	2.11	3.80	0.38	1.97	0.044
S9	578	73.7	3.51	1.90	3.68	0.33	1.98	0.038

as low as 1×10^{-6}. Therefore, the produced DLC/Si system clearly fulfills the requirements of VIMI's operation.

As a first demonstration of this operation, we grew a series of films with small thickness variations. A summary of a representative group (samples S1−S9) is shown in Table 1. We performed fits on their reflectance data and extracted estimates for the film's thickness, the Lorentzian model parameters, and film complex index at 635 nm. In Figure 5, we plot these results, along with additional data for many more samples, including samples of varying thickness (blue diamonds), and of samples exposed either to radiation (green disks) or to vapors of organic contamination (red triangles). The later will be discussed in more detail later. This graph shows the reproducibility of our growth process: excellent correlation between reflectance dip and film thickness, which points to very tight distributions in dielectric function and index at 635 nm. From all the fits (beyond those shown in Table 1) we find that the Lorentzian energy is $\hbar\omega_0 = 3.68 \pm 0.05$ eV, (∼1.5% variation), and the index

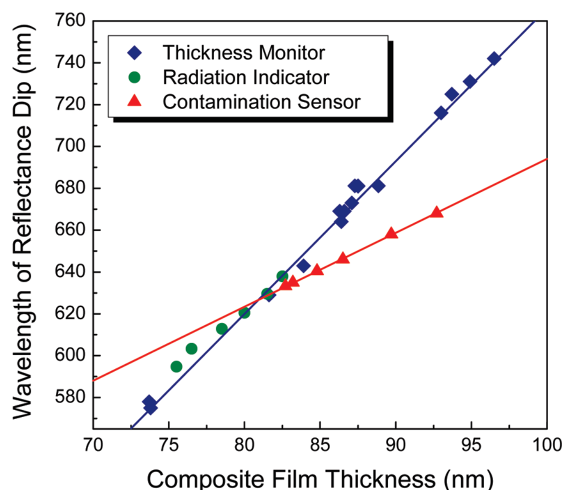

FIGURE 5. Reflectance dips (measured) vs film thickness (fitted) for all samples fabricated and/or processed for the three considered cases: blue diamonds are for different samples with different DLC thickness simulating a thickness monitoring operation, green circles are for a healthy sample exposed to Ar^+ plasma for various times simulating a radiation indicator operation, and red triangles are for a healthy sample undergoing oleic acid adsorption simulating a contamination sensor operation.

at 635 nm is $n_{DLC} = 1.95 \pm 0.02$ (∼1% variation) and $\kappa_{DLC} = 0.035 \pm 0.005$. The other fit parameters of eq 3 were found to be $\varepsilon_\infty = 3.4 \pm 0.1$, $\hbar\gamma = 1.7 \pm 0.2$ eV, and $f = 0.31 \pm 0.03$; these values are consistent with those of various typical DLC films (20, 23, 28).

The next step is to construct the integrated VIMI combining the DLC/Si probe sample and two LEDs (red and green) emitting the spectrum of Figure 2, in the configuration shown in Figure 3. We demonstrate the results of VIMI's use in Figure 6 for samples S1−S9. In Figure 6a, we show their pictures taken at ambient white lighting. The appearance of all samples is characterized by bright blue color without thickness discrimination viewable by bare eye. On the contrary, in Figure 6b, we show their pictures taken in a dark room using VIMI by a Canon IXUS 860 IS camera with a 2 s exposure time. The photocamera has been used for illustration purposes only, because the images are clearly seen by the naked eye in a bright room as well. The transition between green and red appearance for very small thickness variations is clearly seen.

Apart from thickness differences between different samples, this method also gives a single-snapshot topological image of the thickness uniformity of a given sample. For example, samples S4−S6 are nonuniform, and small color variations appear. From Figure 6 and Table 1, we can deduce that with the current scheme we can clearly distinguish thickness differences less than 4 nm by bare eyes; therefore, this scheme can be used as a very sensitive bare-eye thickness monitor for various applications, such as thin film growth on top of the probe sample, making it the reference sample, in a role similar to that of the quartz crystals in microbalance devices. This potential is more clearly and quantitatively demonstrated using Adobe RGB (1998) color image encoding (39). Indeed, Figure 7 shows the RGB coordinates of the images of Figure 6, samples S1−S7, vs the thickness difference from 83 nm (approximately the perfect antireflection thickness for 635 nm, midpoint between samples S1 and S2), for VIMI use (illumination with the spectrum of Figure 2) and white light illumination. For the white light illumination there is no color crossover even for $\Delta t = 15$ nm resulting to common blue appearance. On the other hand, for VIMI use, there is a clear green-red crossover at $\Delta t = 3$ nm demonstrating the increased sensitivity of interferometric effects when the proper light source is used.

As implied in Figure 3, we do not operate under strict normal incidence, but at a small angle. In our setup the distance between source and screen is typically about 10 cm, while the distance between source and sample is around 50 cm, thus the angle of incidence is less than 6°. In Figure 8, we plot the RGB coordinates of the reflected color from a healthy sample as a function of angle of incidence, using Adobe RGB (1998) color image encoding. The RGB values have been determined from photos acquired in $\theta-2\theta$ geometry (mirror reflection) in a goniometer with a 0.1° angular resolution. The insets show the real bare eye appearance of the sample corresponding to several experi-

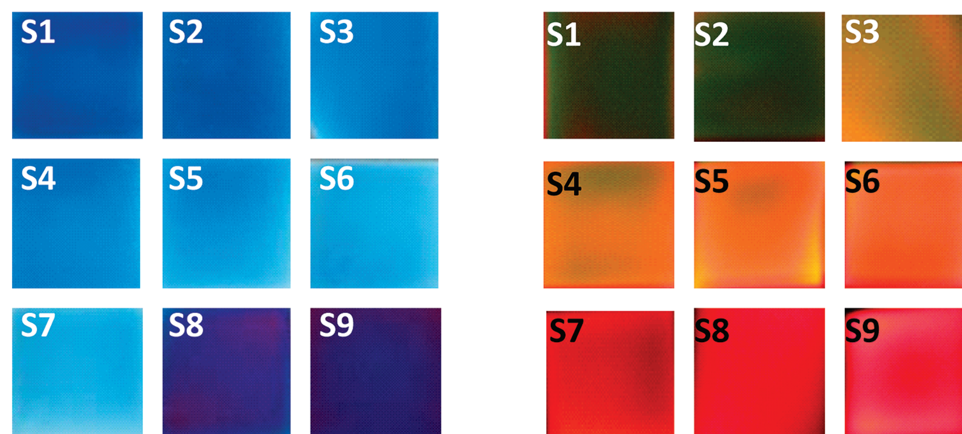

FIGURE 6. Left panel: samples S1−S9 photographed under ambient illumination (white fluorescent lamp). Right panel: samples S1−S9 photographed under illumination with the spectrum of Figure 2 in the configuration of Figure 3. Note that slight thickness variations (sub-nm) of the film thickness can be also viewed in some samples as color variations in the same photograph.

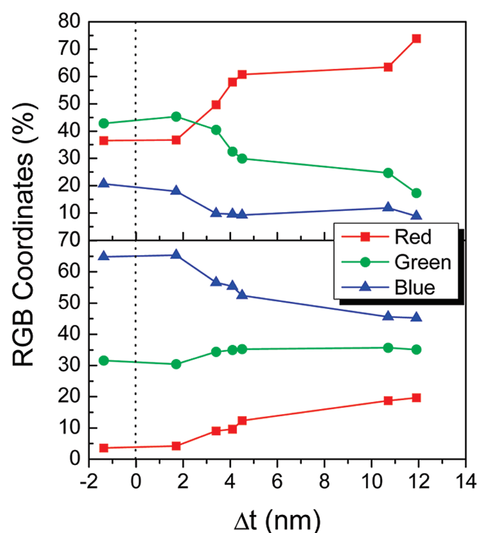

FIGURE 7. RGB coordinates of the images of samples S1−S7 vs the thickness difference from the perfect antireflection thickness (83 nm) for VIMI and white light illumination (the average thickness of samples S1 and S2). Note how the chosen VIMI incident spectrum enhances color crossover and change, compared to that obtained with white light illumination.

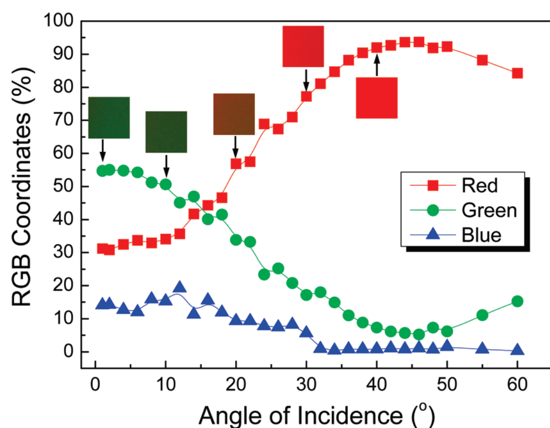

FIGURE 8. RGB coordinates of a healthy DLC/Si sample as a function of incident angle. No visible color change is observed up to 10°, making this the operation limit.

mental points. We note that up to 10° there is no visible color change. Furthermore, we calculate that the unpolarized

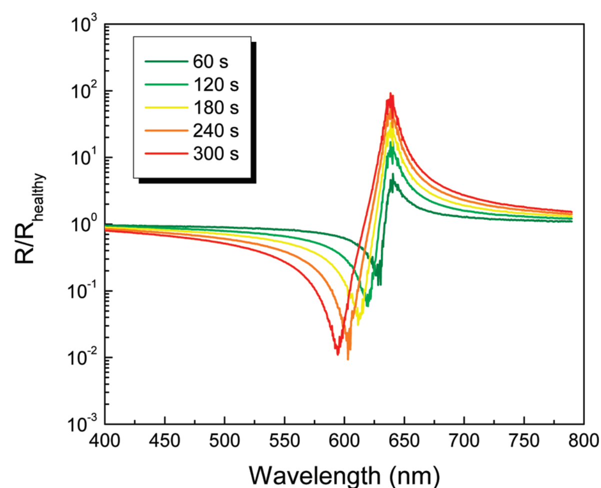

FIGURE 9. Temporal evolution of the reflectance ratio (R-ratio) of DLC/Si, when exposed to Ar^+ plasma. The DLC film thickness reduces due to surface erosion, resulting into a blueshift of the reflectivity dip. Because of the very low reflectance at the healthy state, the reflectance ratio for the etched samples acquires very large values, allowing for quantitative monitoring of sub-nanometer thickness changes.

reflection of a healthy sample starts exceeding 1×10^{-4} at above 12°. Thus, a general rule of $\theta < 10°$ may be suggested for proper operation.

We now turn to a more realistic and interesting space-related application for the VIMI, which is the detection of radiation damage when the DLC/Si probe sample is exposed to plasma or ATOX. To demonstrate this capability, we exposed an optimized DLC/Si probe sample (antireflective at $\lambda = 635$ nm, appearing green when illuminated with the spectrum of Figure 2) to pure Ar^+ plasma and we monitored the evolution of surface erosion. The erosion thickness has been determined by fitting the ORS spectra of the eroded samples using eqs 1 and 3. The spectral position of the reflectance dip is directly correlated with the DLC final film thickness (Figure 5, green disks). This is more clearly illustrated in Figure 9, where the reflectance ratio between the healthy (as grown) DLC/Si probe sample and the samples exposed to plasma for various time intervals are shown. We obtain a very strong anisotropic signal that evolves toward shorter wavelengths with exposure time (the mirror image

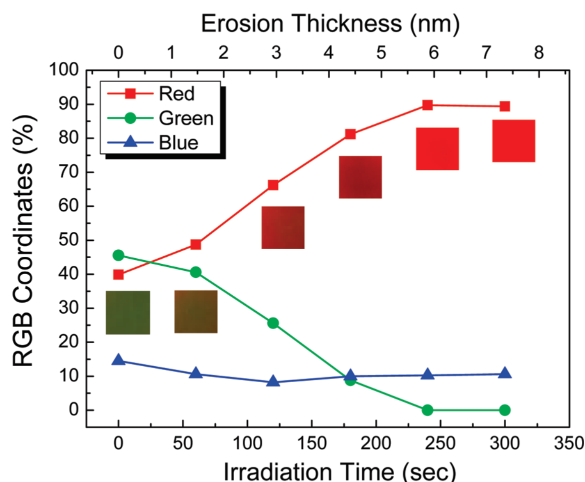

FIGURE 10. RGB coordinates of a series of DLC/Si probe samples exposed to plasma vs the irradiation time and the erosion thickness. For erosion thickness <2.5 nm we observe color crossover and for erosion thickness 6 nm a full color change from green to red takes place. The insets show the real appearance of the reflected beam for each experimental point.

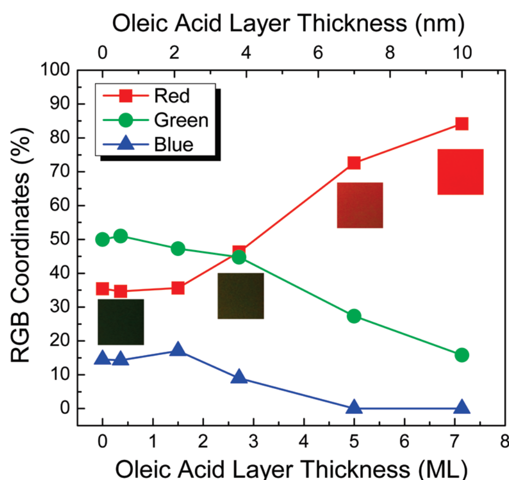

FIGURE 11. Evolution of the RGB coordinates for increasing thickness of the adsorbed oleic acid layer. The oleic acid thickness is fitted by assuming a three-layer system with fixed DLC film thickness and index and fixed oleic acid index, the latter being independently extracted from ORS measurements of thick (>1 cm) oleic acid layer. The insets show the real appearance of the reflected beam for selected experimental points.

of this signal and the opposite shift would appear if there was a thickness increase). Because of the vanishingly small reflectance of the healthy sample, the peak reflectance ratio acquires large values even for the smallest thickness change (a ratio ~5 for the smallest exposure time of 60 s, or $\Delta t \approx$ 1.5 nm). With proper calibration this allows quantitative subnanometer resolution. Visually, on the other hand, this is manifested into a changed appearance for the probe sample from green (for the healthy condition and for 60 s exposure time), to red (for 300 s exposure time).

These results are again quantified by using the Adobe RGB (1998) color image encoding. In Figure 10 we correlate the erosion thickness, determined by the spectroscopic ORS method, with the RGB coordinates of the reflected beam from the VIMI; the insets show the real bare eye appearance of each sample corresponding to every experimental point. In this case, the VIMI is even more sensitive in color crossover than in the cases of Figure 7 and achieves clear bare-eye color discrimination for thickness changes as low as 2.5 nm. For thickness change of 6 nm we observe a full color inversion from clear green to pure red. We stress again here that obtaining thickness changes by fitting the ORS data requires sophisticated equipment and analysis, whereas with a proper calibration of Figure 10, they become bare-eye accessible.

The final demonstration of VIMI is for the most demanding space-related application, that of an organic contamination sensor. For this purpose we exposed a DLC/Si probe sample to saturated vapors of oleic acid (analytical grade); fat acids, such as oleic acid or stearic acid, can be adsorbed on carbonaceous surfaces and their detection is extremely demanding and usually requires sophisticated equipment and analysis tools (42). We performed reflectivity and transmission analysis on a thick (>1 cm) layer of oleic acid and extracted its refractive index in the visible as $n_{\text{oleic}} = 1.465 + 17.3/\lambda$, $\kappa_{\text{oleic}} < 1 \times 10^{-12}$. With fixed the DLC index and layer thickness, we fit the ORS spectra of the composite DLC+oleic system to get the adsorbed oleic acid thickness. The reflectance dips vs the composite film thickness (DLC+ oleic acid thickness) are shown in Figure 6. Regarding the visual appearance of the DLC/Si probe sample used as organic contamination sensor, in Figure 11 we demonstrate the evolution of the RGB coordinates for increasing thickness of the adsorbed oleic acid layer. The color crossover takes place below 3 monolayers of adsorbed oleic acid (~4 nm). A full color inversion from green to red takes place at less than <10 nm or 7 monolayers of adsorbed oleic acid.

These striking results extend the human ability to look at the nanoscale with bare eyes and directly observe thickness changes of a few nanometers without the intervention of any kind of interface, using just the appropriate probe template (DLC/Si) and illumination. Although the visual inspection of calibrated color changes is necessarily semiquantitative and cannot possibly compete in resolution to other highly sophisticated methods, its simplicity and speed of assessment may prove crucial in a variety of applications and disciplines.

5. SUMMARY AND CONCLUSIONS

We have presented a new design for an interferometric multi-indicator, which is consisting of a DLC/Si probe sample and two LEDs (green and red). The DLC/Si probe sample is antireflective (reflectance $< 1 \times 10^{-4}$) at $\lambda = 635$ nm (red) and in the healthy condition reflects only the green light ($\lambda = 535$ nm). This device changes color when an infinitesimal thickness change is taking place due to erosion (e.g., exposure to plasma or ATOX) or to adsorption of an organic contaminant. We have demonstrated that with this device we can detect with bare eyes changes on the order of <4 nm for erosion and <5 molecular layers (~7 nm) of an adsorbed organic contaminant without the aid of any kind of instrumental or numerical interface.

ARTICLE

Acknowledgment. The authors gratefully acknowledge Prof. G.A. Evangelakis for fruitful discussions and support in realizing this work. This work has been supported by the European Space Agency (ESA) under Contract 21071/07/NL/PA.

REFERENCES AND NOTES

(1) Hariharan, P. *Handbook of Optics*; McGraw Hill: New York, 1996.
(2) Morgan, C. *Nature* **1986**, *324*, 293–293.
(3) Matsumoto, H.; Hirai, A. *Opt. Commun.* **1999**, *170*, 217–220.
(4) Bozhevolnyi, S. I.; Volkov, V. S.; Devaux, E.; Laluet, J.-Y.; Ebbesen, T. W. *Nature* **2006**, *440*, 508–511.
(5) Casiraghi, C.; Hartschuh, A.; Lidorikis, E.; Qian, H.; Harutyunyan, H.; Gokus, T.; Novoselov, K. S.; Ferrari, A. C. *Nano Lett.* **2007**, *7*, 2711–2717.
(6) Lezec, H. J.; McMahon, J. J.; Nalamasu, O.; Ajayan, P. M. *Nano Lett.* **2007**, *7*, 329–333.
(7) van Delft, K. M.; Eijkel, J. C. T.; Mijatovic, D.; Druzhinina, T. S.; Rathgen, H.; Tas, N. R.; van den Berg, A.; Mugele, F. *Nano Lett.* **2007**, *7*, 345–350.
(8) Ymeti, A.; Greve, J.; Lambeck, P. V.; Wink, T.; van Hövell, S. W. F. M.; Beumer, T. A. M.; Wijn, R. R.; Heideman, R. G.; Subramaniam, V.; Kanger, J. S. *Nano Lett.* **2007**, *7*, 394–397.
(9) Hÿtch, M.; Houdellier, F.; Hüe, F.; Snoeck, E. *Nature* **2008**, *453*, 1086–1089.
(10) Conroy, M.; Mansfield, D. *Nat. Photonics* **2008**, *2*, 661–663.
(11) Jiang, Y.; Tang, C. *Rev. Sci. Instrum.* **2008**, *79*, 106105.
(12) Madani-Grasset, F.; Pham, N. T.; Glynos, E.; Koutsos, V. *Mater. Sci. Eng., B* **2008**, *152*, 125–131.
(13) Xu, Z.; Shilpiekandula, V.; Youcef-Toumi, K.; Yoon, S. F. *Opt. Express* **2009**, *17*, 15104–15117.
(14) Packirisamy, S.; Schwam, D.; Litt, M. H. *J. Mater. Sci.* **1995**, *30*, 308–320.
(15) Peters, P. N.; Gregory, J. C.; Swann, J. T. *Appl. Opt.* **1986**, *25*, 1290–1298.
(16) Grossman, E.; Gouzman, L.; Lempert, G.; Noter, Y.; Lifshitz, Y. *J. Spacecr. Rockets* **2004**, *41*, 356–359.
(17) Ueda, M.; Takahashi, W. K.; Marcondes, A. R.; Tan, I. H.; Silva, G. *AIP Conf. Proc.* **2009**, *1087*, 691–703.
(18) Wurz, P.; Saul, L.; Scheer, J. A.; Möbius, E.; Kucharek, H.; Fuselier, S. A. *J. Appl. Phys.* **2008**, *103*, 054904.
(19) Robertson, *J. Mater. Sci. Eng., R* **2002**, *37*, 129–281.
(20) Kassavetis, S.; Patsalas, P.; Logothetidis, S.; Robertson, J.; Kennou, S. *Diamond Relat. Mater.* **2007**, *16*, 1813–1822.
(21) Waidmann, S.; Knupfer, M.; Fink, J.; Kleinsorge, B.; Robertson, J. *J. Appl. Phys.* **2001**, *89*, 3783–3792.
(22) Theye, M.-L.; Paret, V.; Sadki, A. *Diamond Relat. Mater.* **2001**, *10*, 182–190.
(23) Fanchini, G.; Tagliaferro, A.; Dowling, D. P.; Donnely, K.; McConnell, M. I.; Flood, R.; Lang, G. *Phys. Rev. B* **2000**, *61*, 5002–5010.
(24) Heitz, T.; Godet, C.; Bouree, J. E.; Drevillon, B.; Conde, J. P. *Phys. Rev. B* **1999**, *60*, 6045–6052.
(25) Canillas, A.; Pollo, M. C.; Andújar, J. L.; Sancho, J.; Bosch, S.; Robertson, J.; Milne, W. I. *Diamond Relat. Mater.* **2001**, *10*, 1132–1136.
(26) Lee, J.; Collins, R. W.; Veerasamy, V. S.; Robertson, J. *Diam. Relat. Mater.* **1998**, *7*, 999–1009.
(27) Katsuno, T.; Godet, C.; Orlianges, J. C.; Loir, A. S.; Garrelie, F.; Catherinot, A. *Appl. Phys. A: Mater. Sci. Process.* **2005**, *81*, 471–476.
(28) Schwarz-Selinger, T.; von Keudell, A.; Jacob, W. *J. Appl. Phys.* **1999**, *86*, 3988–3996.
(29) Jellison, G. E.; Merkulov, V. I.; Puretzky, A. A.; Geoneghan, D. B.; Eres, G.; Lowndes, D. H.; Caughman, J. B. *Thin Solid Films* **2000**, *377–378*, 68–73.
(30) Casiraghi, C.; Ferrari, A. C.; Robertson, J. *Phys. Rev. B* **2005**, *72*, 085401.
(31) Vercammen, K.; Meneve, J.; Dekempeneer, E.; Smeets, J.; Roberts, E. W.; Eiden, M. J. *Surf. Coat. Technol.* **1999**, *120–121*, 612–617.
(32) Donnet, C.; Fontaine, J.; Le Mogne, T.; Belin, M.; Héau, C.; Terrat, J. P.; Vaux, F.; Pont, G. *Surf. Coat. Technol.* **1999**, *120–121*, 548–554.
(33) Baker, C. C.; Chromik, R. R.; Wahl, K. J.; Hu, J. J.; Voevodin, A. A. *Thin Solid Films* **2007**, *515*, 6737–6743.
(34) Voevodin, A. A.; Zabinski, J. S. *Compos. Sci. Technol.* **2005**, *65*, 741–748.
(35) Semikina, V. T.; Shmyryeva, A. N. *Diamond Relat. Mater.* **2002**, *11*, 1329–1331.
(36) Vercammen, K.; Meneve, J.; Dekempeneer, E.; Roberts, E. W.; Eiden, M. J. *Proceedings of the 9th European Space Mechanisms and Tribology Symposium*; Liège, Belgium, Sept 19–21; European Space Agency: Paris, 2001; *ESA SP-480*, 309.
(37) Patsalas, P.; Logothetidis, S. *J. Appl. Phys.* **2003**, *93*, 989–999.
(38) http://www.prolight.com.
(39) http://www.adobe.com/digitalimag/adobergb.html.
(40) Ferrari, A. C.; Libassi, A.; Tanner, B. K.; Stolojan, V.; Yuan, J.; Brown, L. M.; Rodil, S. E.; Kleinsorge, B.; Robertson, J. *Phys. Rev. B* **2000**, *62*, 11089.
(41) Wooten, F. *Optical Properties of Solids*; Academic Press: New York, 1972.
(42) Zafeiropoulos, N. E.; Vickers, P. E.; Baillie, C. A.; Watts, J. F. *J. Mater. Sci.* **2003**, *38*, 3903–3914.

AM100532B